Supplementary Information

Anchored oxygen-retardant phase stabilizing high-voltage Ni-rich cathode materials

Ziqi Liu[1#], Yiming Zhang[1#], Yong Chen[2#], Meng Yao[1*], Yangyang Wang[1], Du Yuan[3], Haitao Zhang[4], Yun Zhang[1*], and Guoxiu Wang[2*]

Keywords: Ni-rich cathode, anchored oxygen-retardant phase, oxygen emission, structural stability, high-voltage

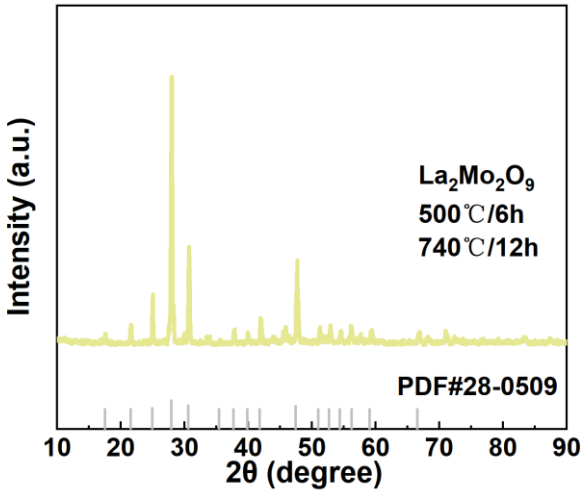

Figure S1. XRD pattern of β-La2Mo2O9 (LMO) obtained using optimized La/Mo ratio and sintering process.

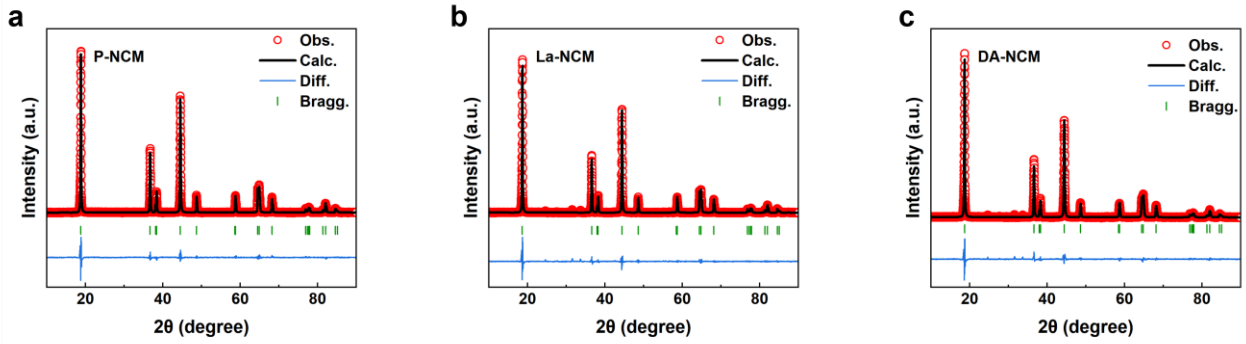

Figure S2. XRD Rietveld refinement for P-NCM (a), La-NCM (b) and DA-NCM (c).

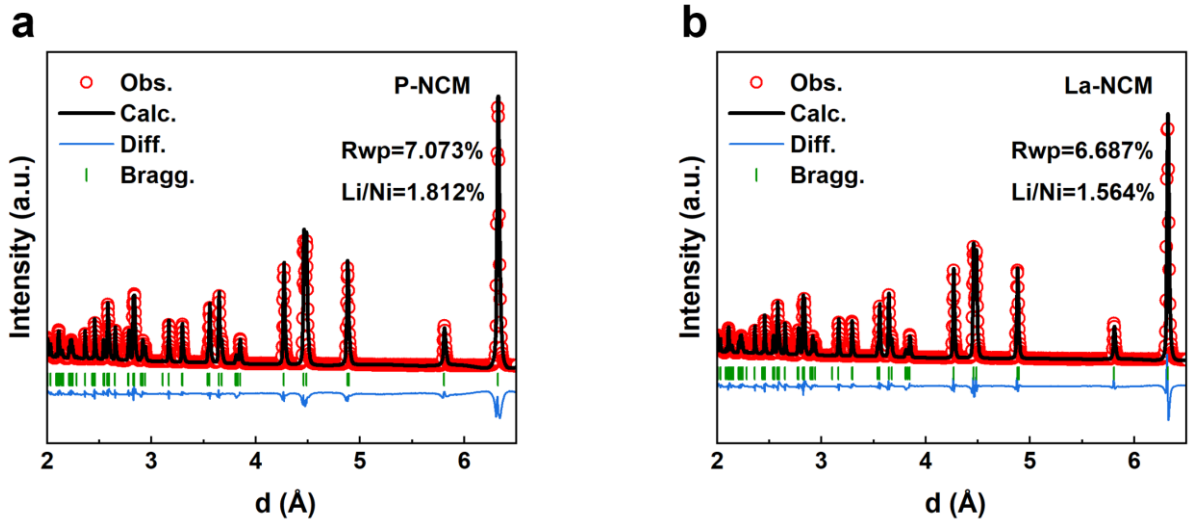

Figure S3. NPD Rietveld refinement for P-NCM (a), La-NCM (b).

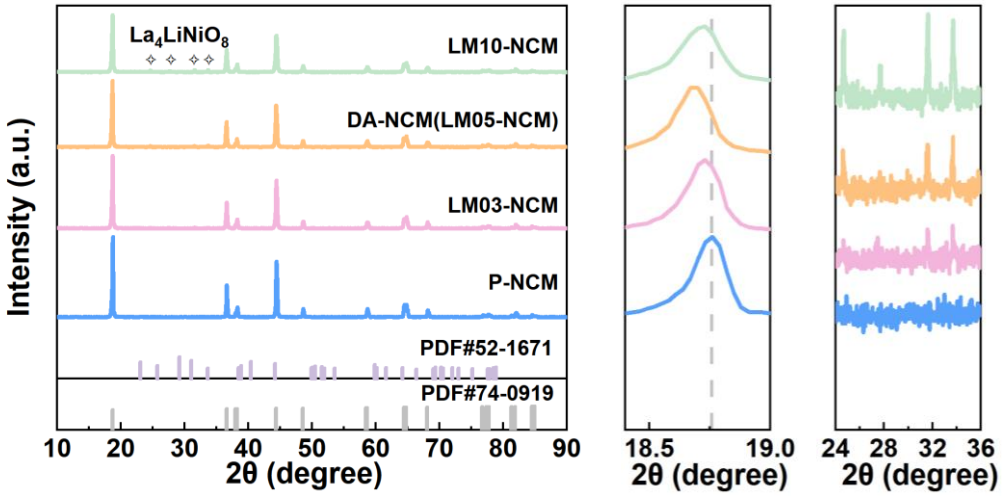

Figure S4. XRD patterns for P-NCM and different ratios modified samples at a fast scan rate of 9° min^{-1} .

The zoom peaks on the right figures show that the 003 peak shifts to a lower angle and there are obvious LLNO diffraction peaks after the anchored strategy. Besides, anchored strategy reduces Li/Ni mixing compared with P-NCM, La-NCM and Mo-NCM.

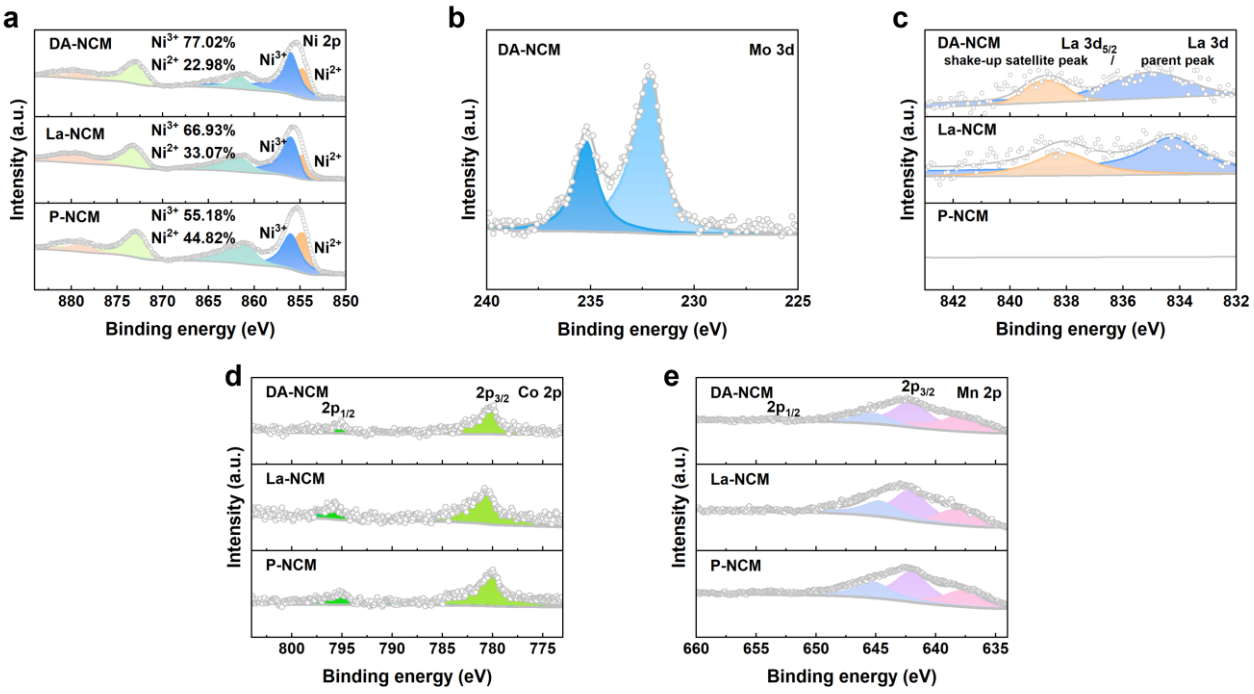

Figure S5. XPS data of Ni 2p (a), Mo 3d (b), La 3d (c), Co 2p (d) and Mn 2p (e) taken from the surface of all the samples.

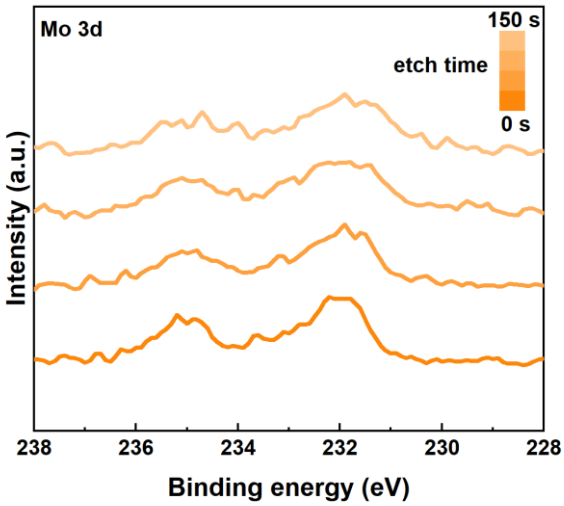

Figure S6. XPS depth profiles Mo 3d of DA-NCM as a function of Ar etching time from 0 s to 150 s.

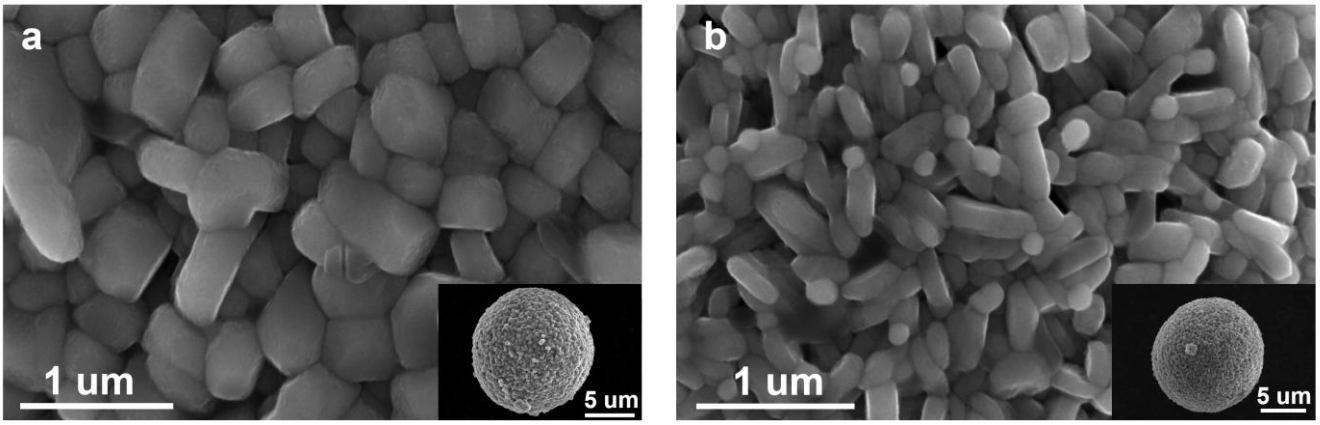

Figure S7. SEM images of P-NCM (a) and DA-NCM (b).

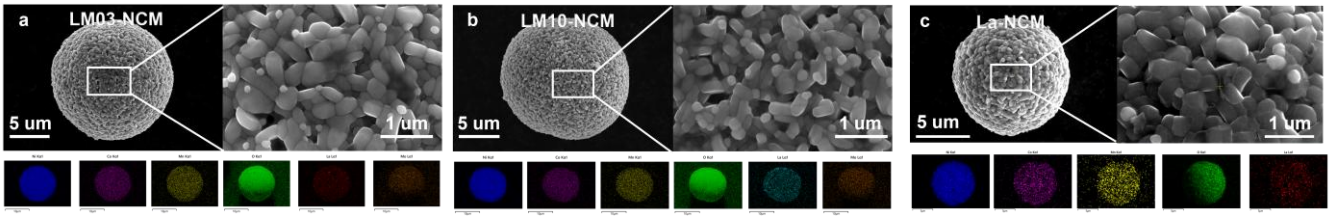

Figure S8. SEM and corresponding mapping images for LM03-NCM (a), LM10-NCM (b) and La-NCM (c).

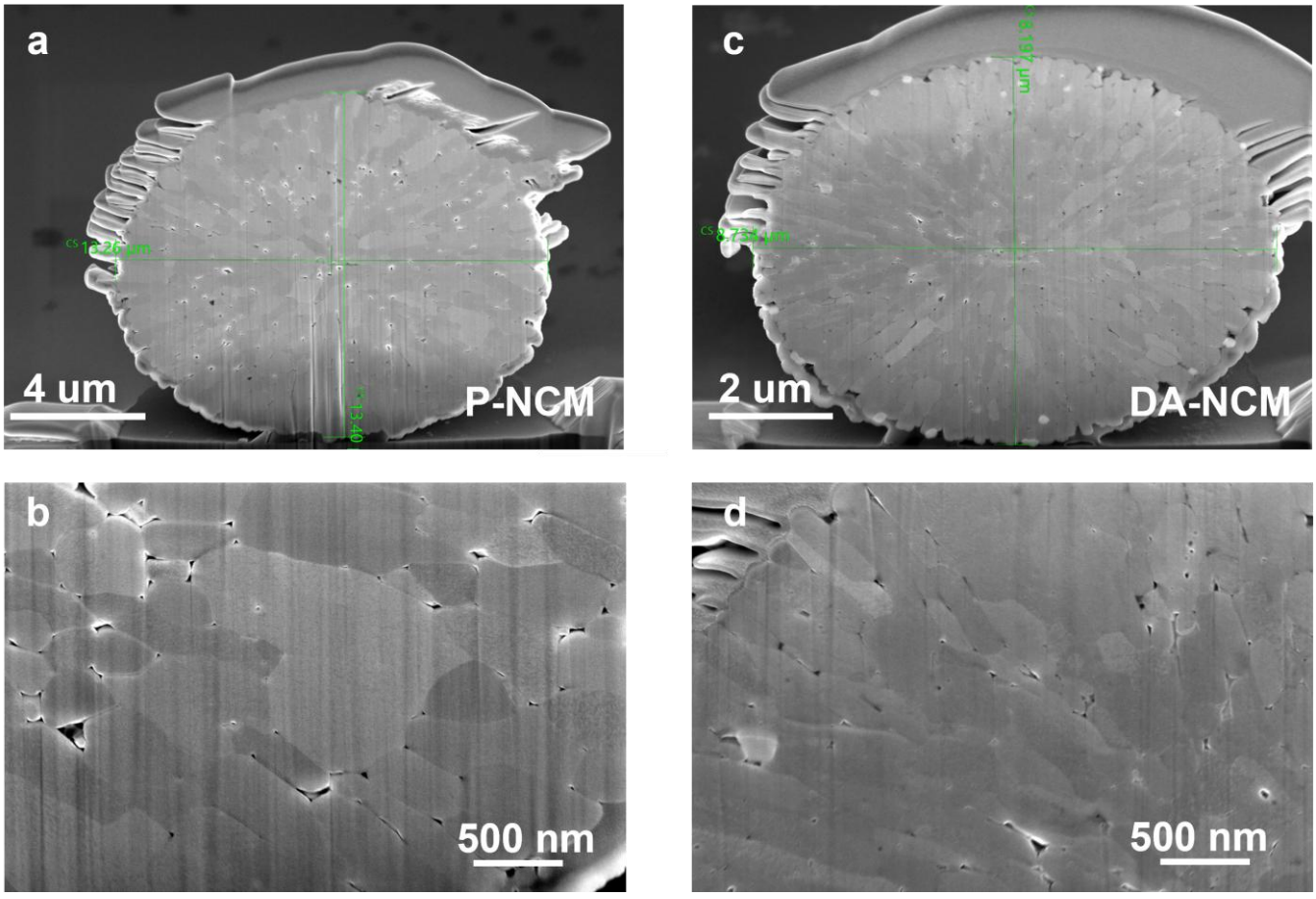

Figure S9. Cross-sectional FIB-SEM images of P-NCM (a, b) and DA-NCM (c, d).

The secondary particle size of DA-NCM is significantly reduced, and the primary particle is refined, meanwhile, the intergranular pores are reduced.

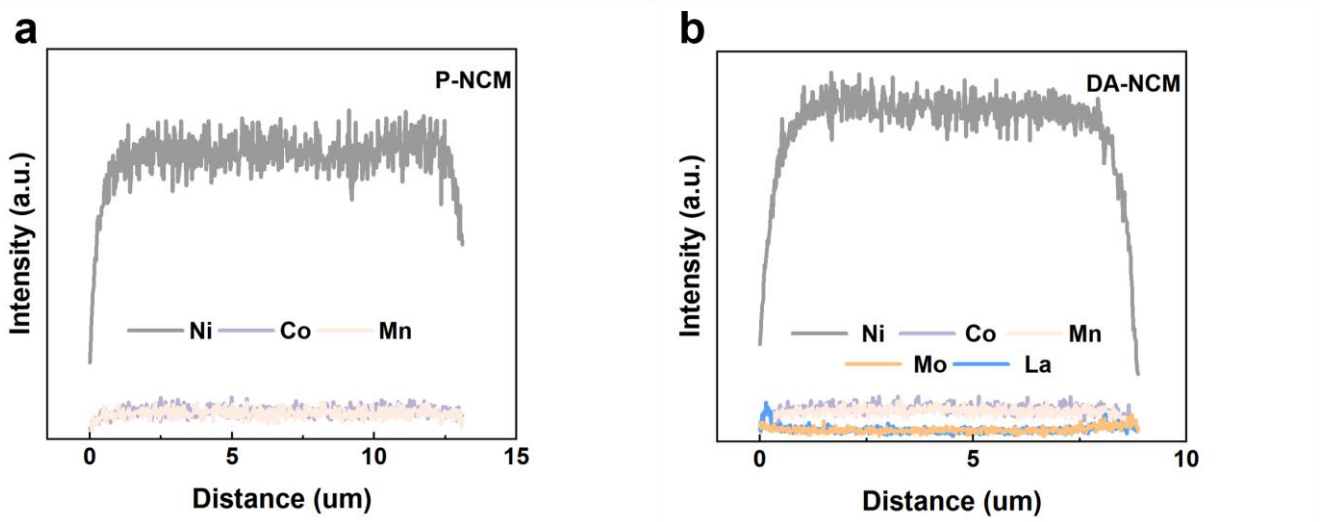

Figure S10. The corresponding elements distribution on the cross-sectioned for P-NCM (a) and DA-NCM (b).

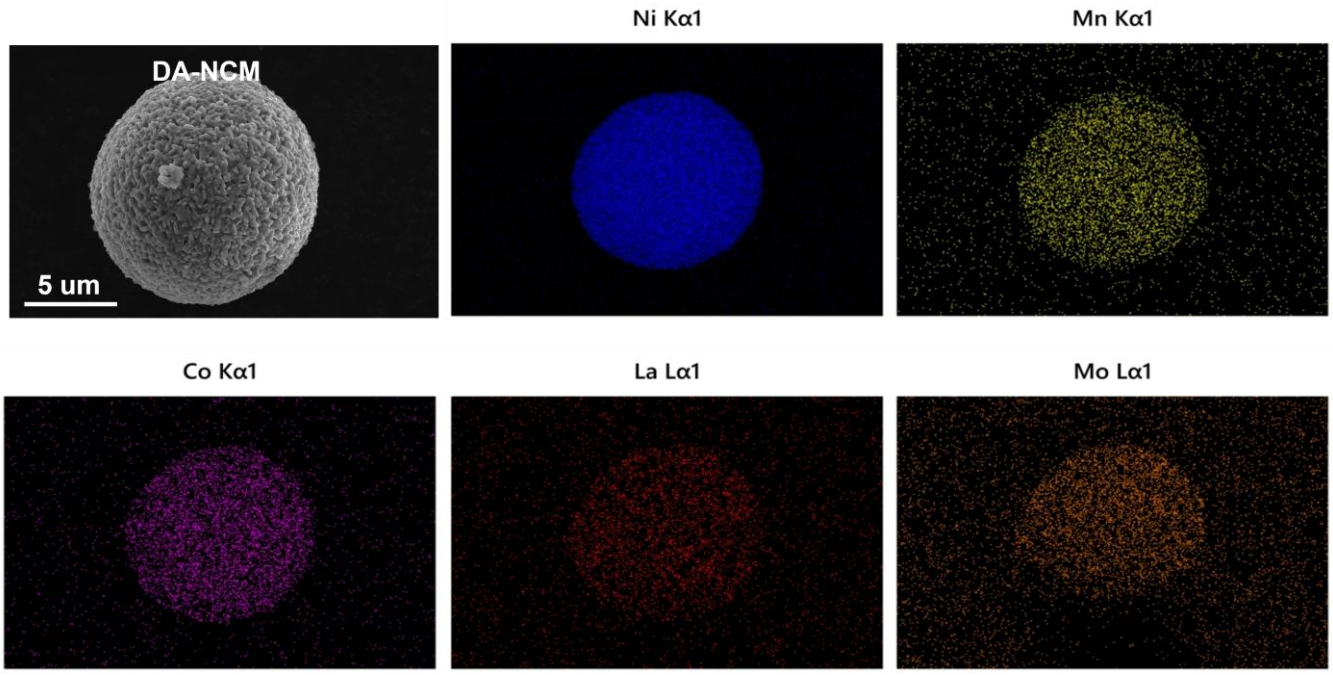

Figure S11. EDS mapping images of DA-NCM.

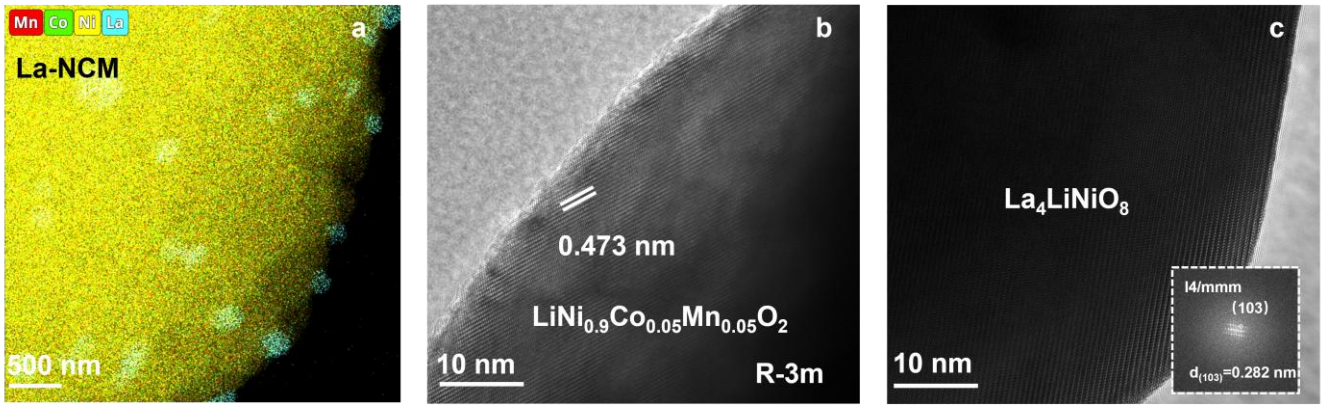

Figure S12. Element distribution (a) and TEM images (b, c) of La-NCM.

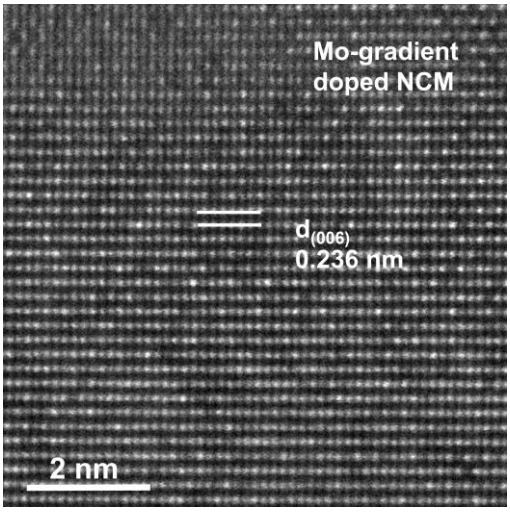

Figure S13. AC-STEM images of Mo gradient doping on the DA-NCM surface.

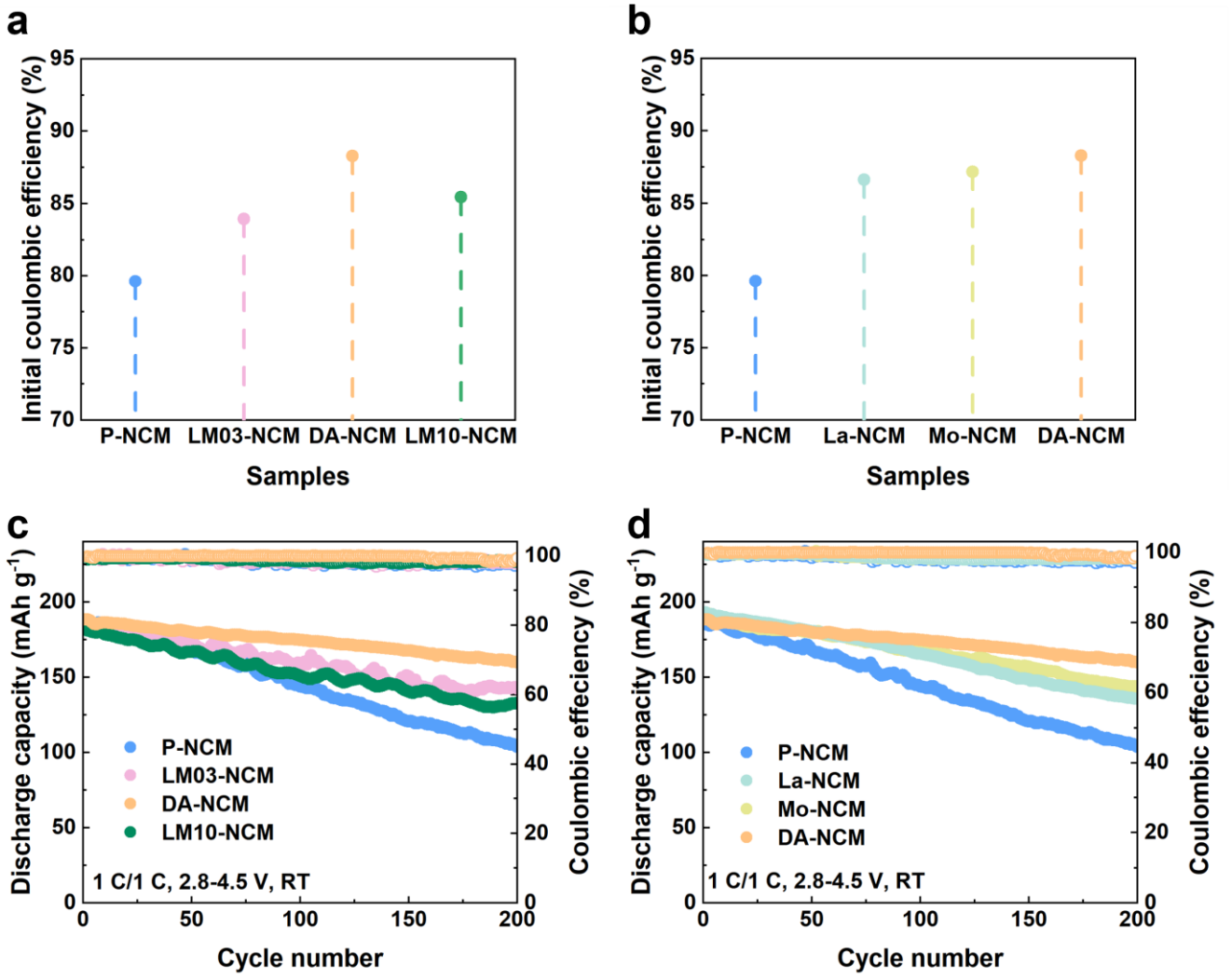

Figure S14. Initial coulombic efficiency and cycling performance of DA-modified (a, c) and simple-modified (b, d). samples.

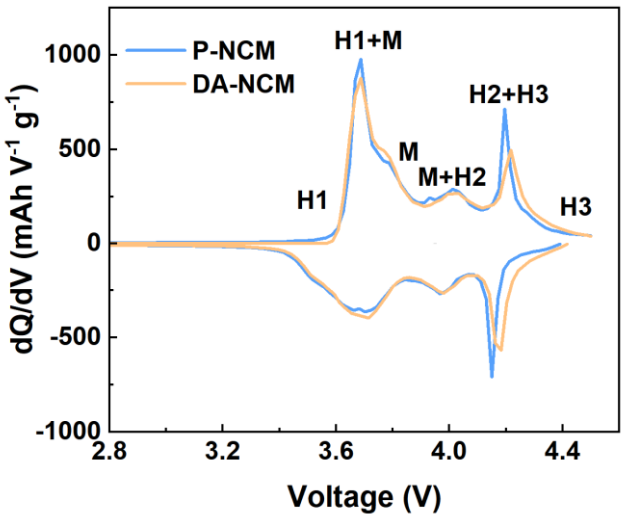

Figure S15. dQ/dV curves of P-NCM and DA-NCM at the first cycle.

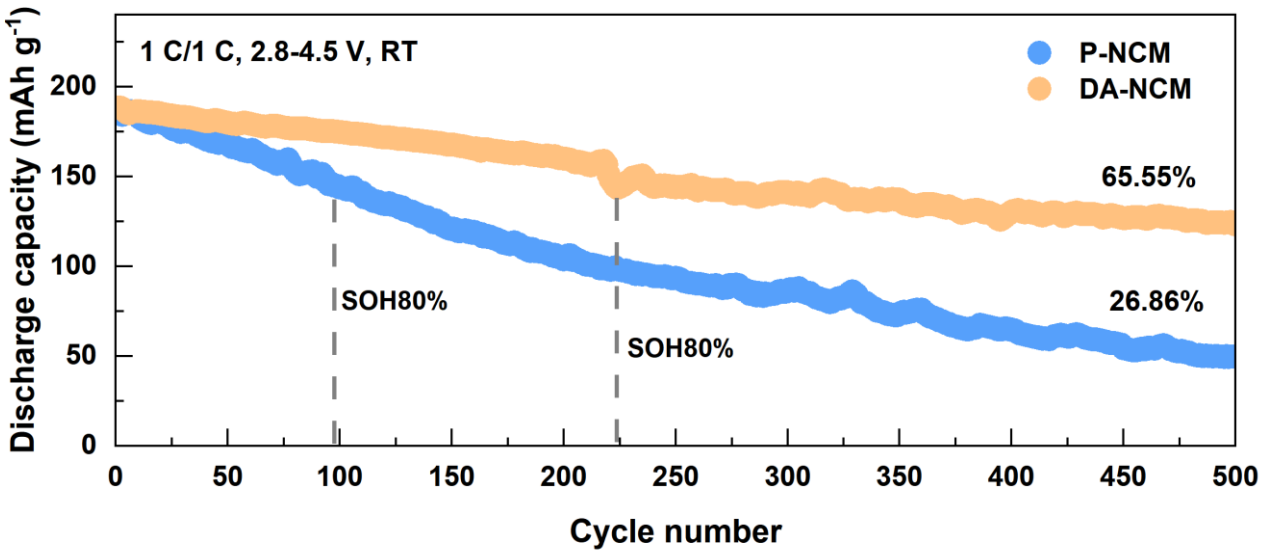

Figure S16. Cycle performance of P-NCM and DA-NCM after a long-time charge/discharge under high voltage.

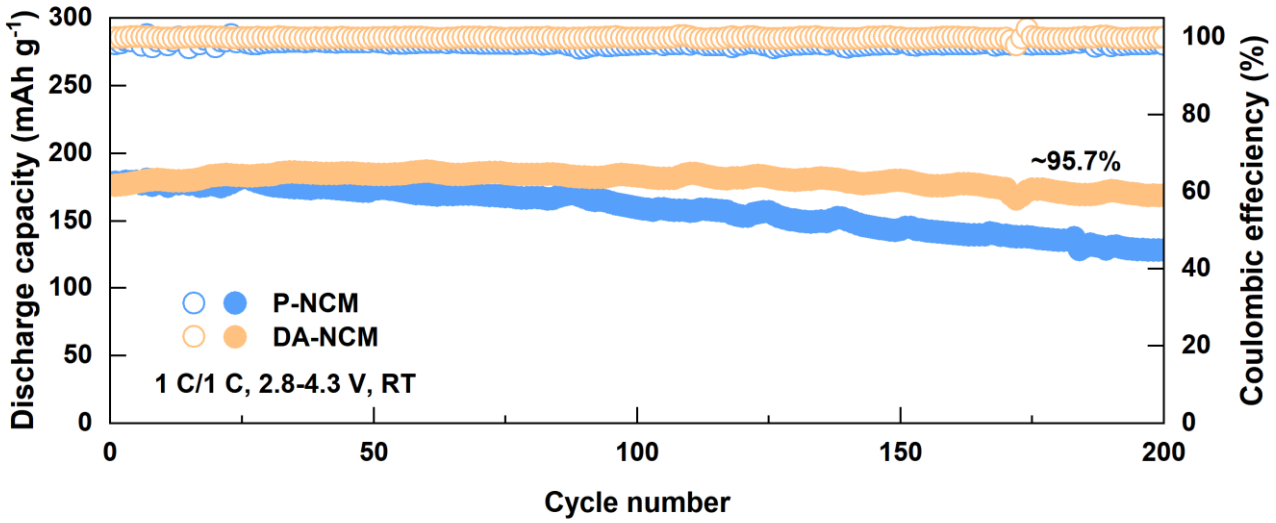

Figure S17. Cycle performance of DA-NCM under 2.8-4.3 V at 1C.

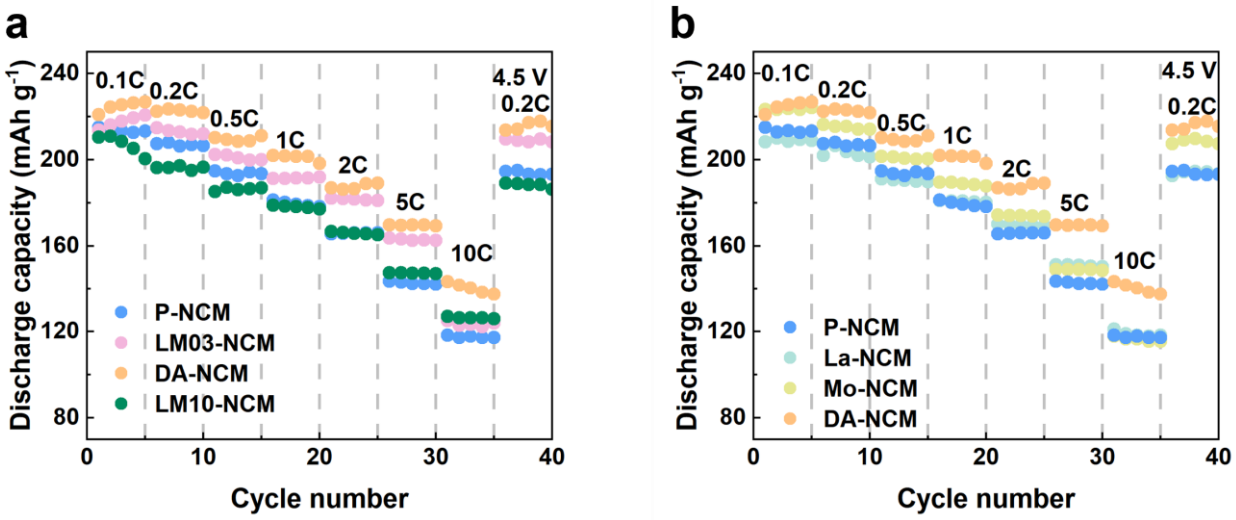

Figure S18. Rate performance of DA-modified (a) and simple-modified (b) samples.

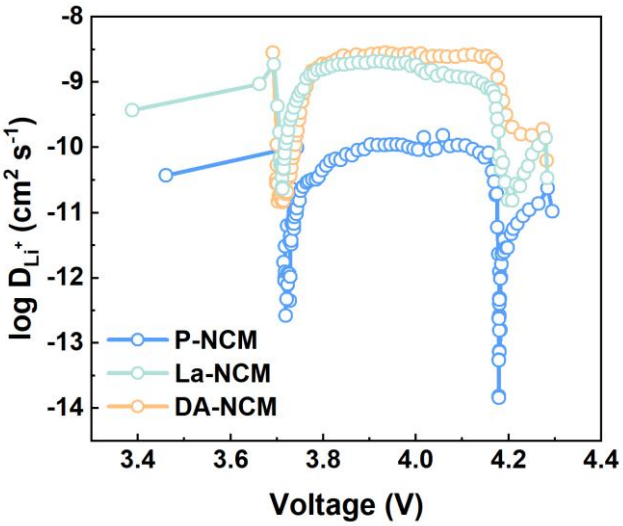

Figure S19. GITT curves of P-NCM, La-NCM and DA-NCM.

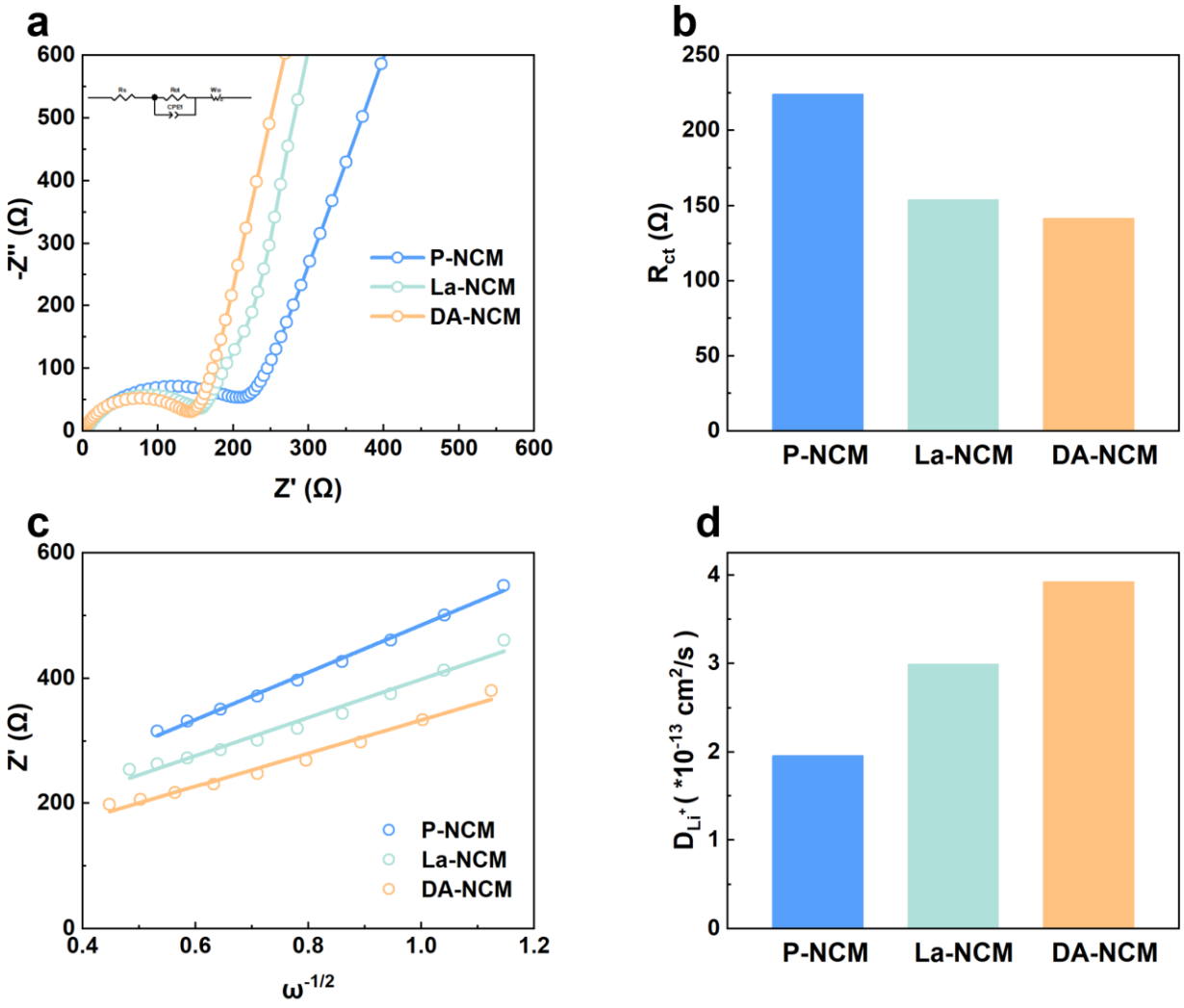

Figure S20. Nyquist plots for P-NCM, La-NCM and DA-NCM before cycling (a) and corresponding Rct values (b).

Z'-$\omega^{-1/2}$ image (c) and the lithium-ion diffusion coefficient (d).

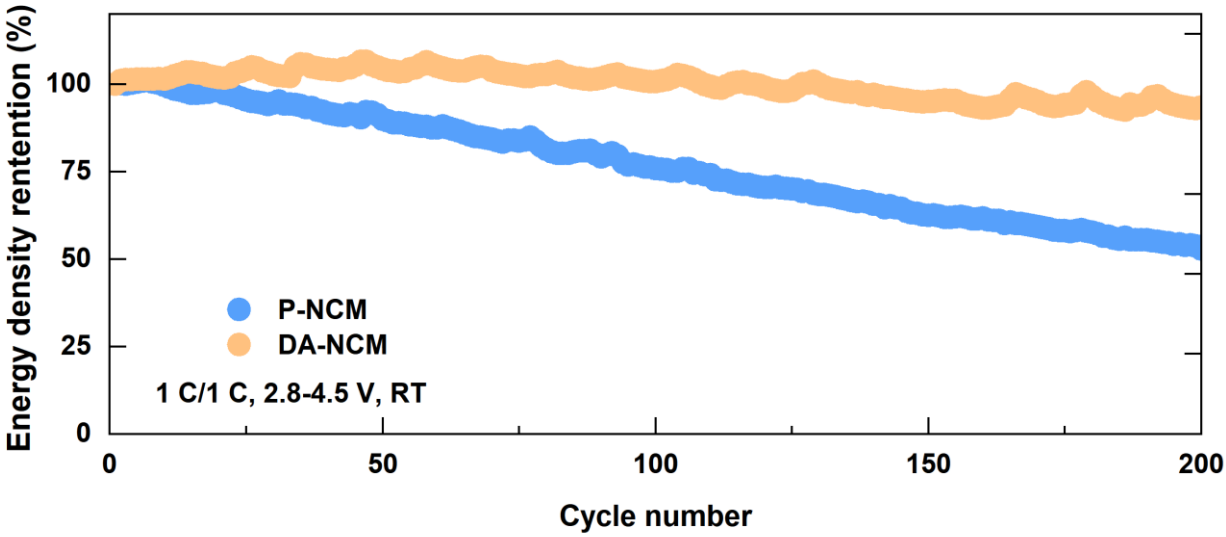

Figure S21. Energy density retention of P-NCM and DA-NCM under 2.8-4.5 V at 1 C.

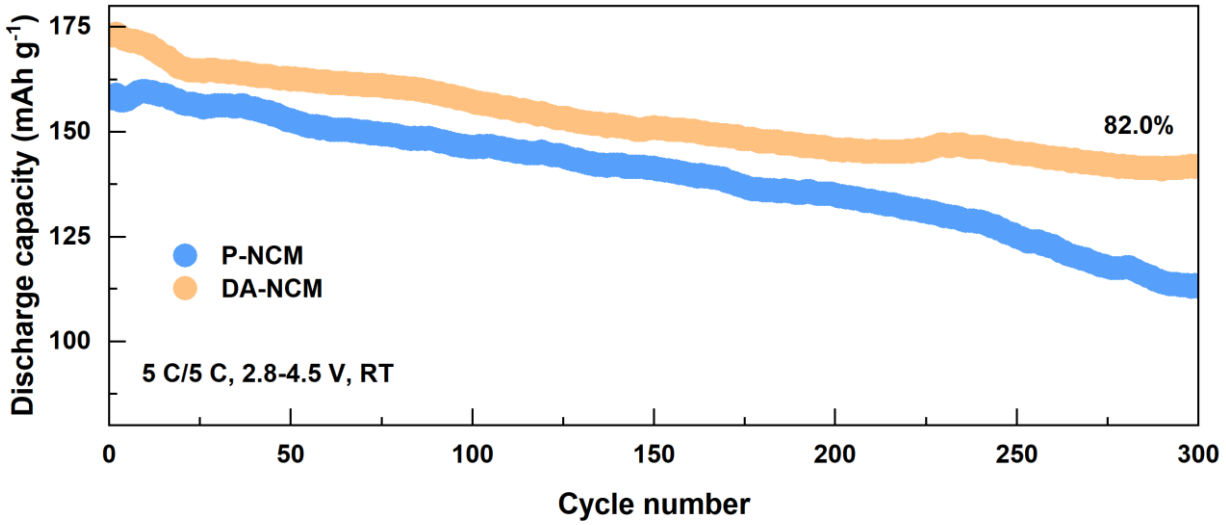

Figure S22. Fast charging performance of P-NCM and DA-NCM under 2.8-4.5 V at 5C.

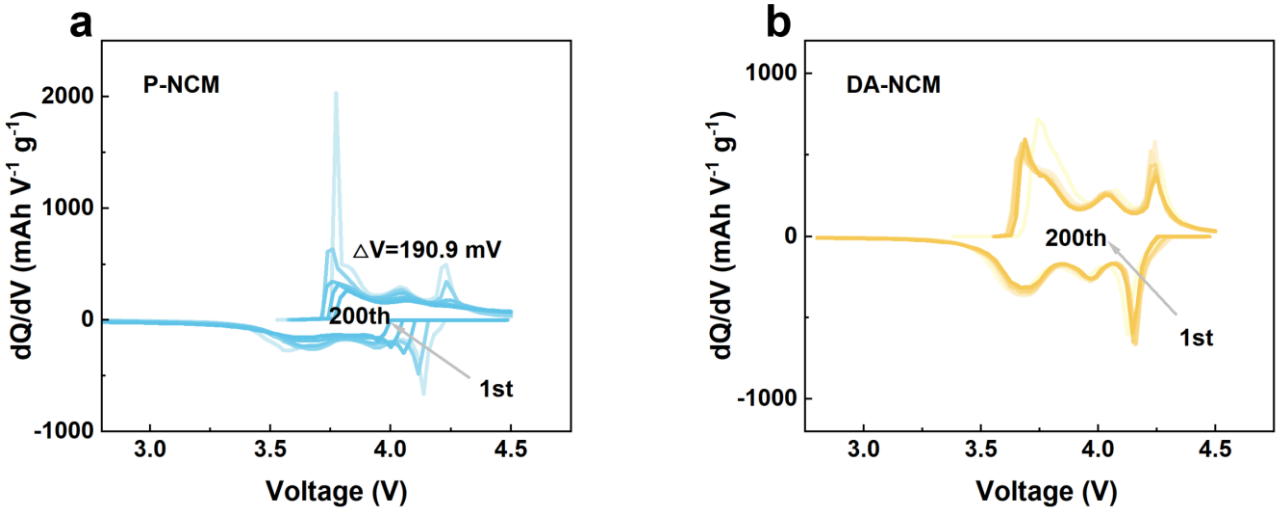

Figure S23. dQ/dV curves of P-NCM (a) and DA-NCM (b) under 2.8-4.5 V at 1 C.

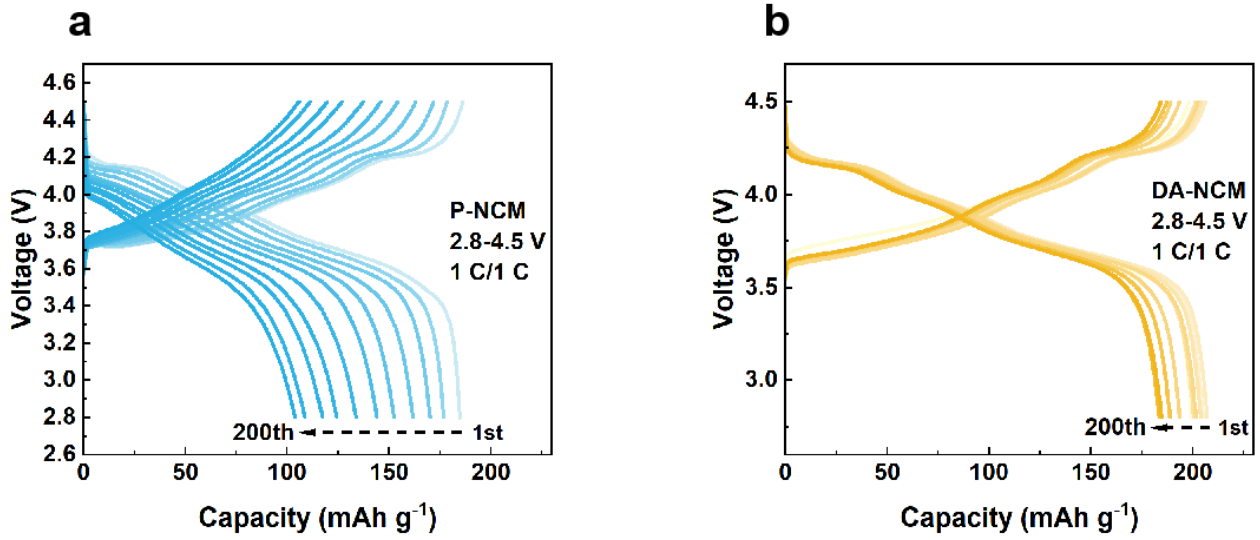

Figure S24. Charge/discharge profiles of P-NCM (a) and DA-NCM (b) under 2.8-4.5 V at 1 C.

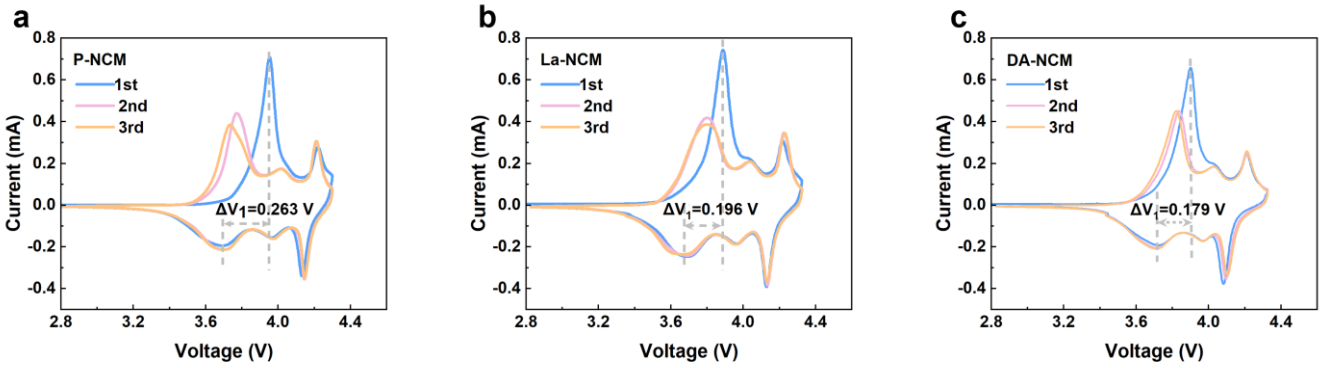

Figure S25. CV curves of P-NCM (a), La-NCM (b) and DA-NCM (c).

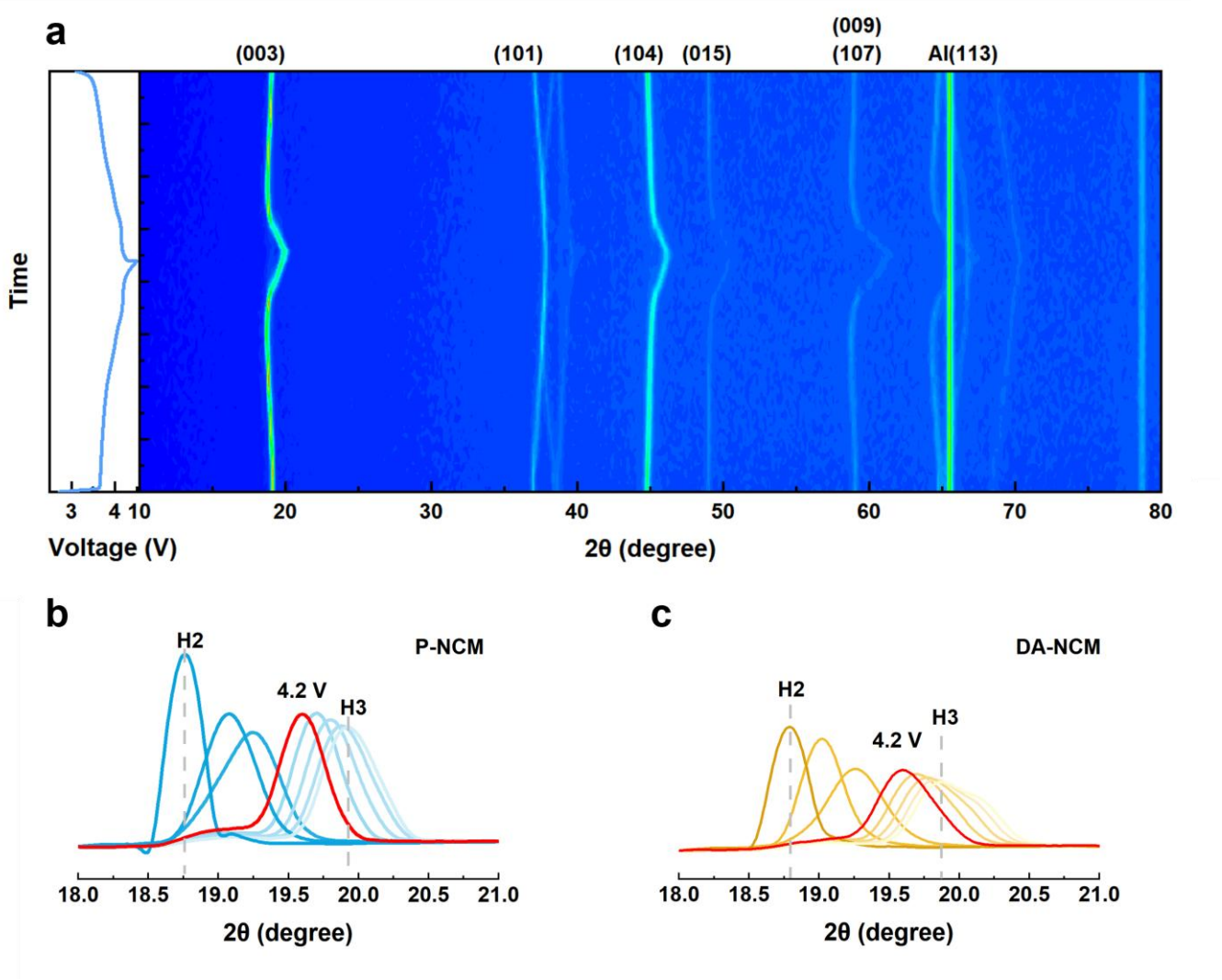

Figure S26. Full range contour plot of in-operando XRD data on P-NCM during the first cycle (a). The enlarged (003) peak of P-NCM (b) and DA-NCM (c) during the first charge.

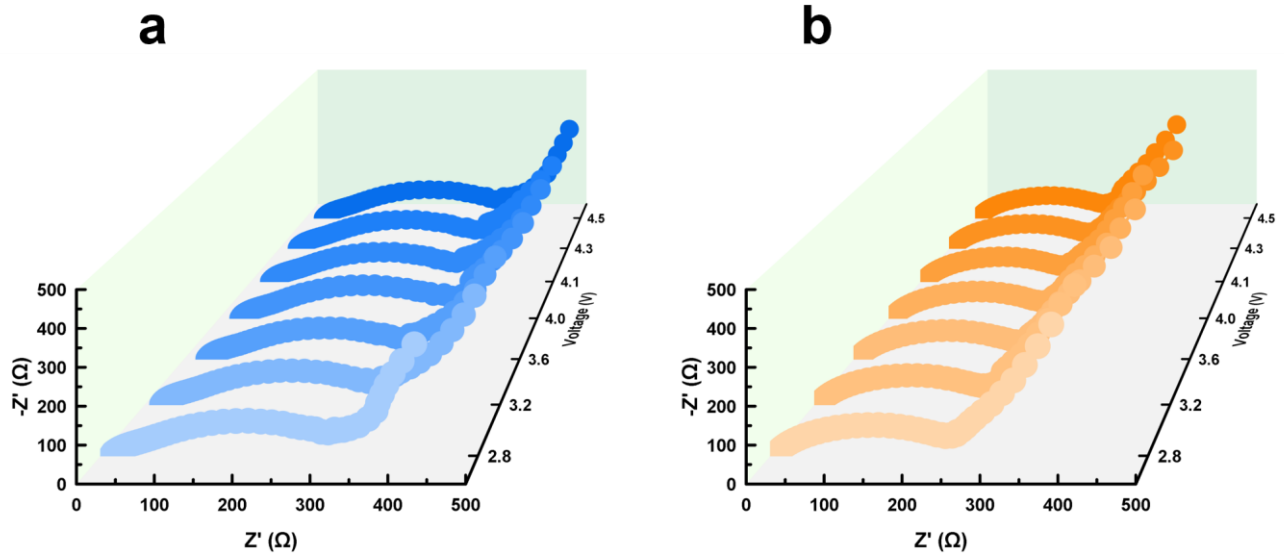

Figure S27. The in-situ galvanostatic electrochemical impedance spectroscopy plots of P-NCM (a) and DA-NCM (b).

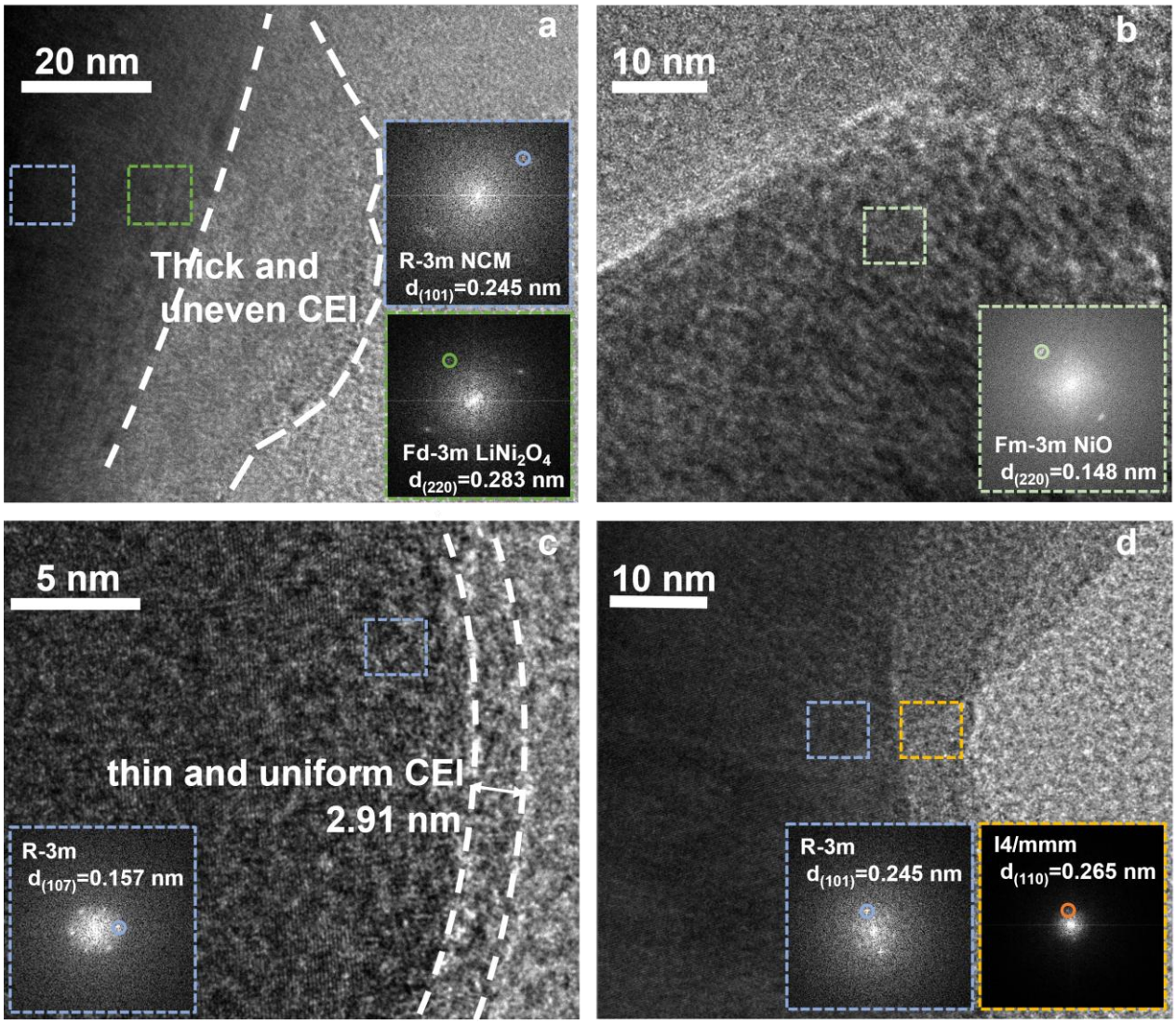

Figure S28. HR-TEM images of the CEI and the structural evolution of P-NCM (a, b) and DA-NCM (c, d) after cycling.

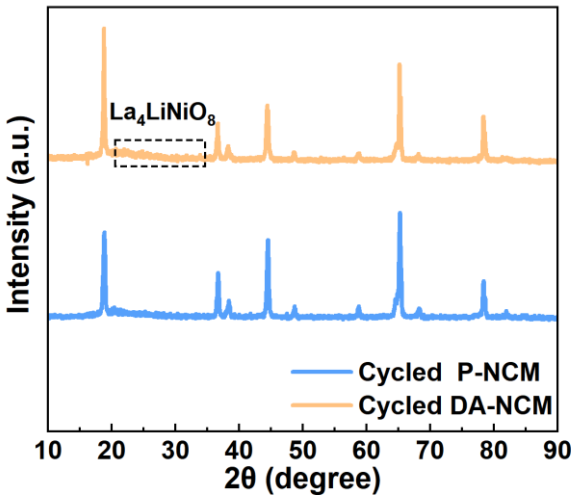

Figure S29. XRD patterns of P-NCM and DA-NCM after cycling.

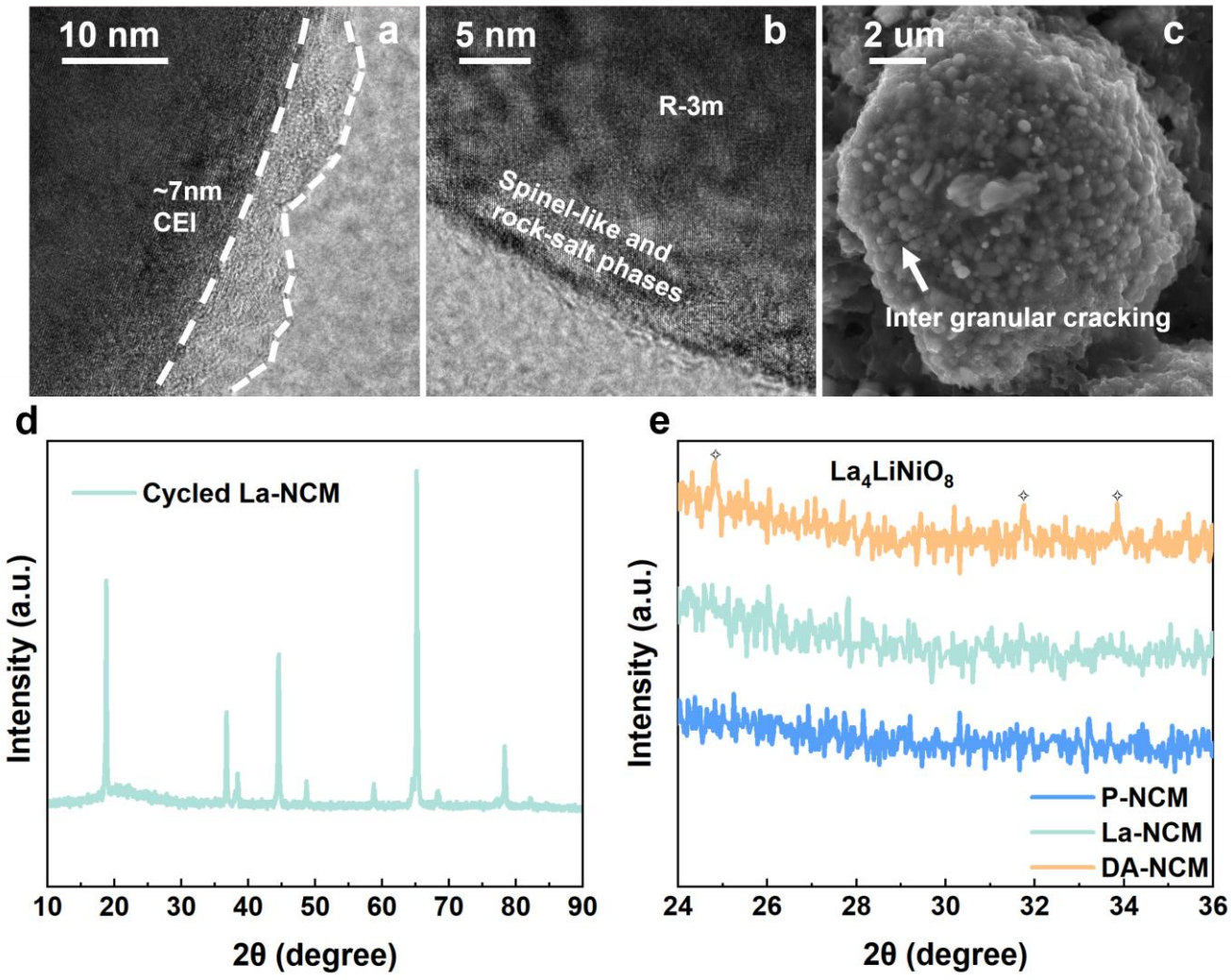

Figure S30. CEI image (a), HR-TEM image of structural evolution (b) and SEM image (c) of La-NCM after cycling.

(d) XRD patterns of La-NCM after high rate cycling (e) The comparison XRD patterns after high rate cycling of P-NCM, La-NCM and DA-NCM.

These cycled-La-NCM tests confirm that although La-NCM could enhance the structural stability to some extent, spinel and salt rock phases still appear on the surface after long cycling, and the CEI is thicker than that of DA-NCM. In addition, cracks could be observed on the particles after high-rate cycling of La-NCM, and the characteristic LLNO peaks are no longer visible after cycling, suggesting that the LLNO coating is detached from the NCM surface after long cycling.

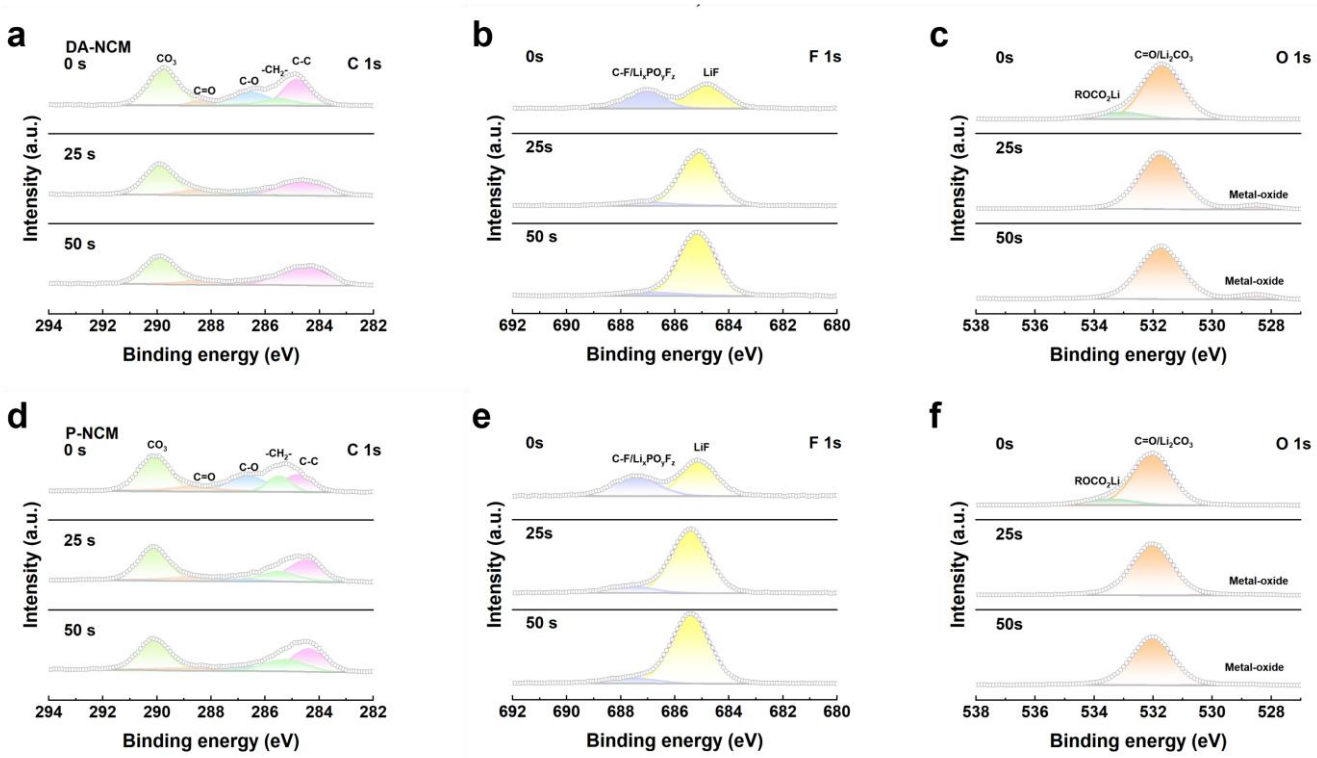

Figure S31. Ar-etched XPS data of DA-NCM (a-c) and P-NCM (d-f) after cycling.

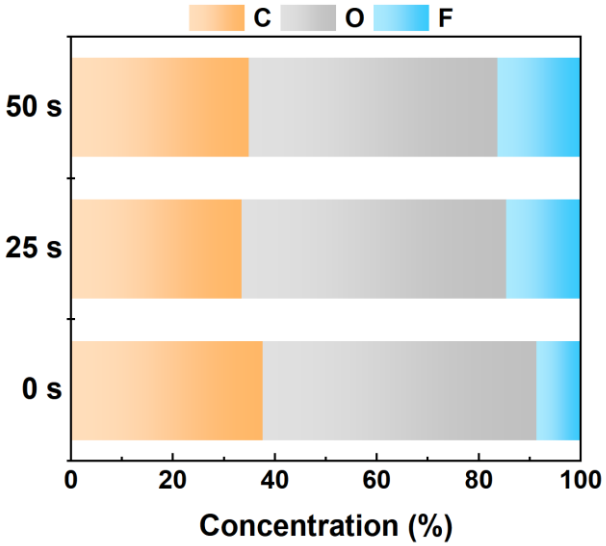

Figure S32. C, O and F atomic concentrations of P-NCM after cycling.

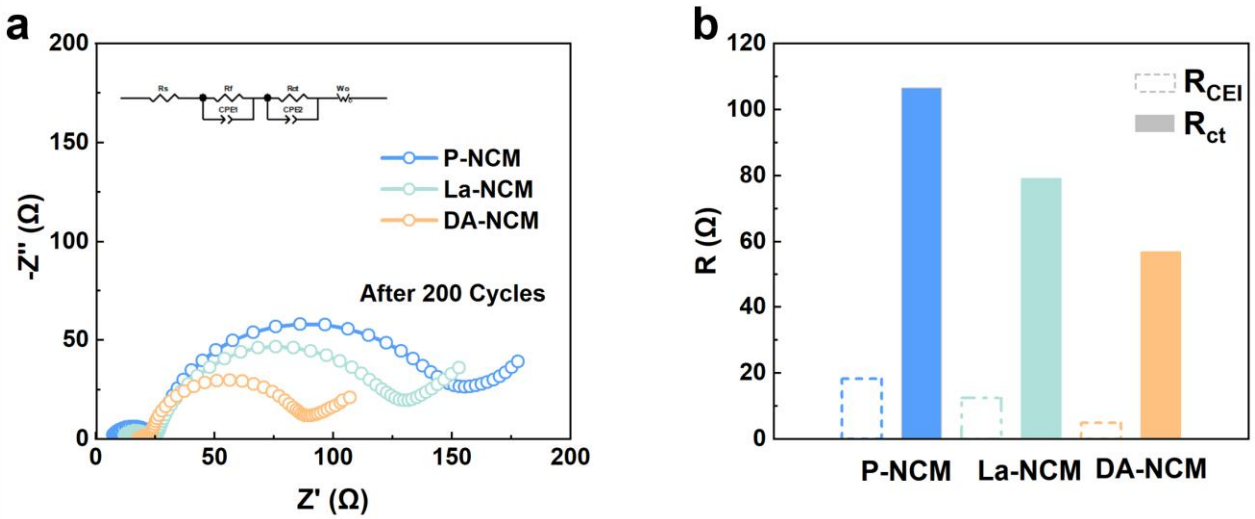

Figure S33. Nyquist plots for P-NCM, La-NCM and DA-NCM after cycling (a) and corresponding R_{ct} and R_{CEI} values (b).

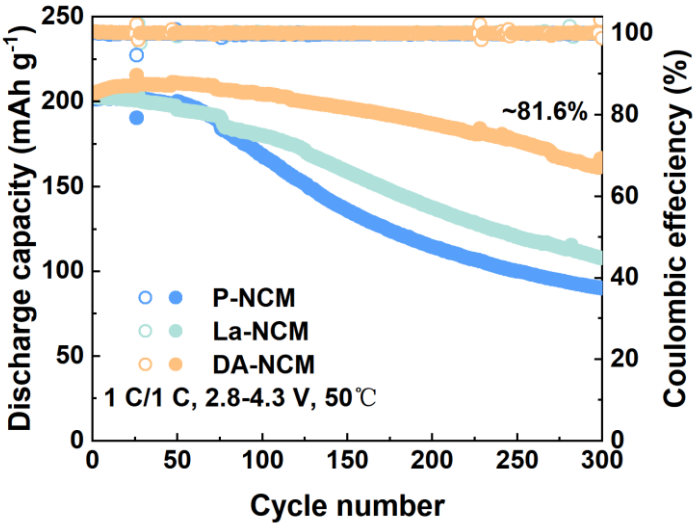

Figure S34. Cycling performance of P-NCM, La-NCM and DA-NCM under 2.8–4.3 V at 50°C.

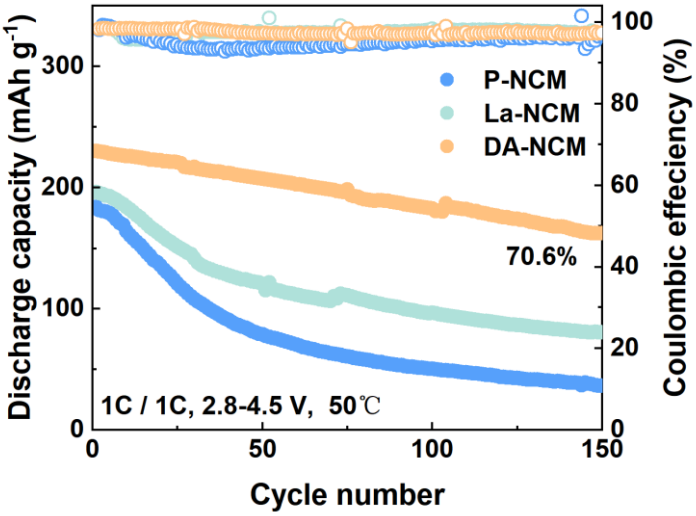

Figure S35. Cycling performance of P-NCM, La-NCM and DA-NCM under 2.8–4.5 V at 50°C.

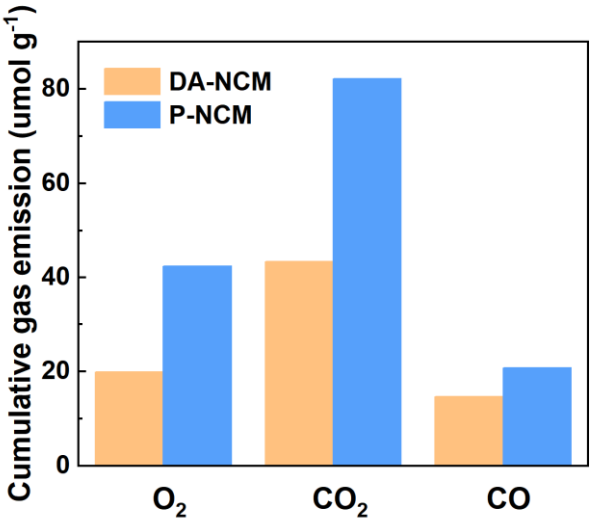

Figure S36. Comparative graph of cumulative gas emissions based on DEMS test results.

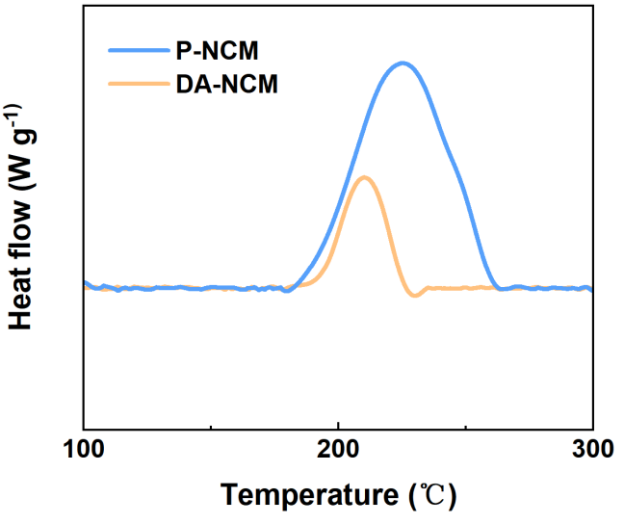

Figure S37. DSC test of P-NCM and DA-NCM.

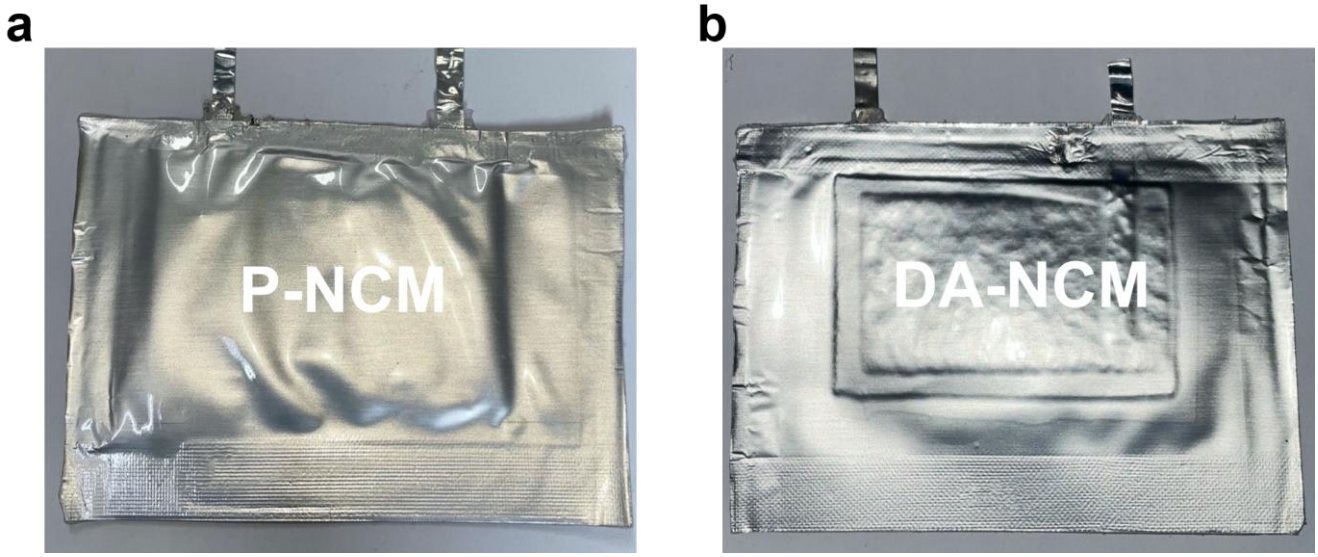

Figure S38. Pouch cells of P-NCM (a) and DA-NCM (b) after the initial charge/discharge under 2.8-4.5 V at 50℃.

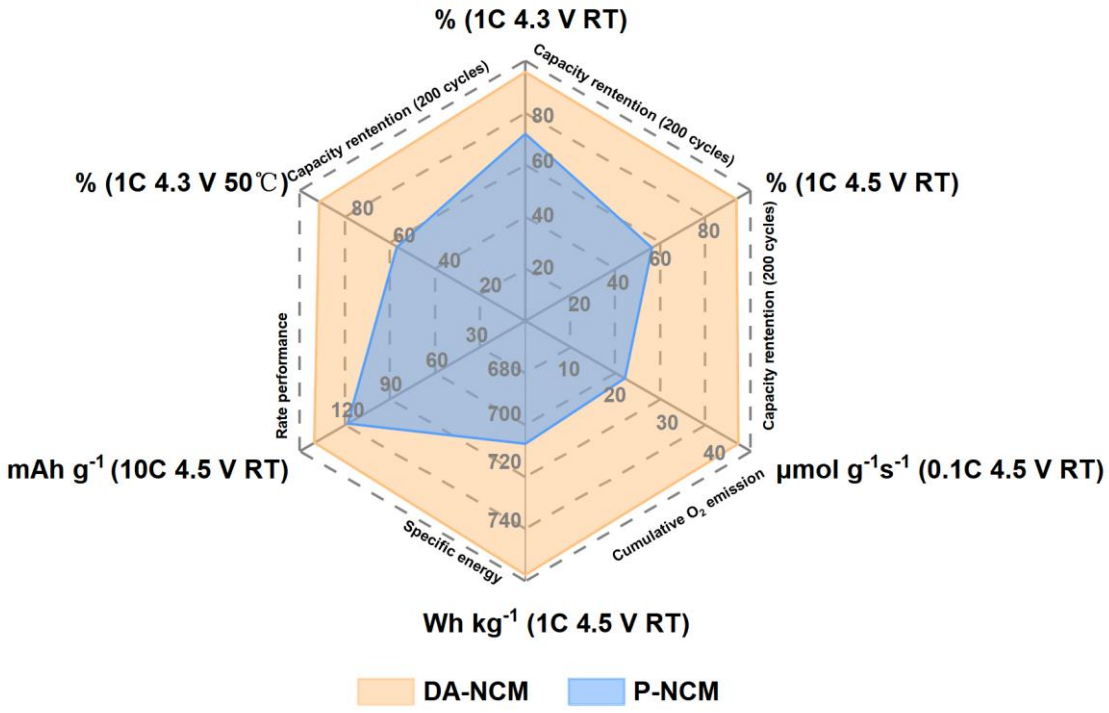

Figure S39.Comparison of P-NCM and DA-NCM.

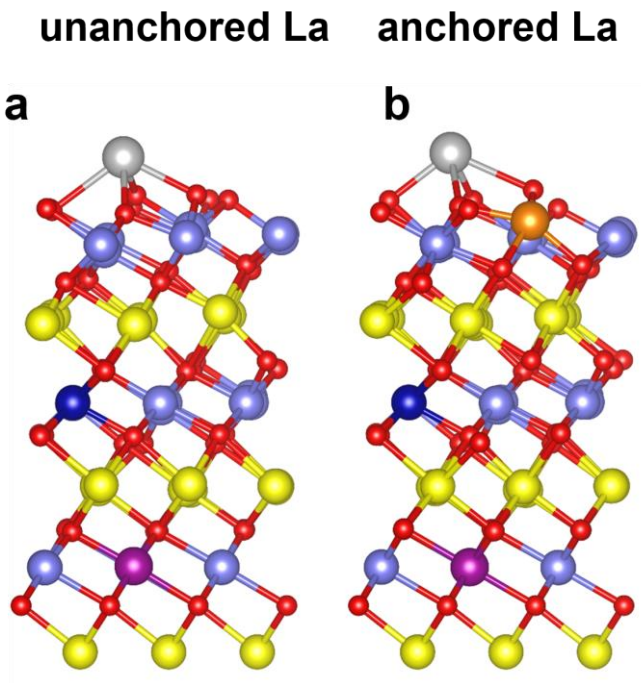

Figure S40. Optimized structure between NCM surface and La and Mo, unanchored La-O structure in La-NCM (a) and anchored La-O structure in DA-NCM (b).

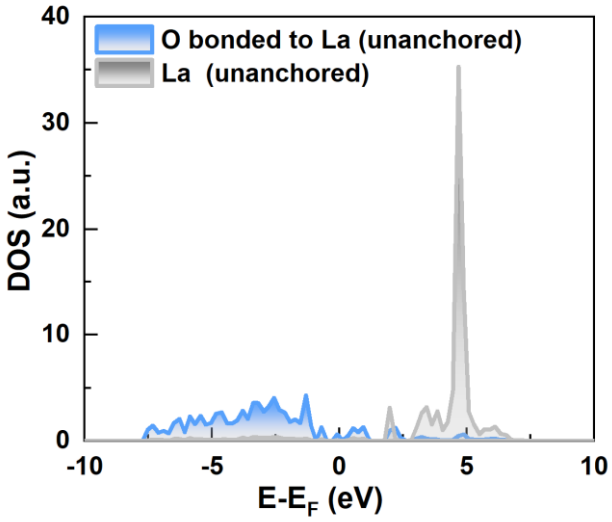

Figure S41. Density of states for the unanchored La-O structure.

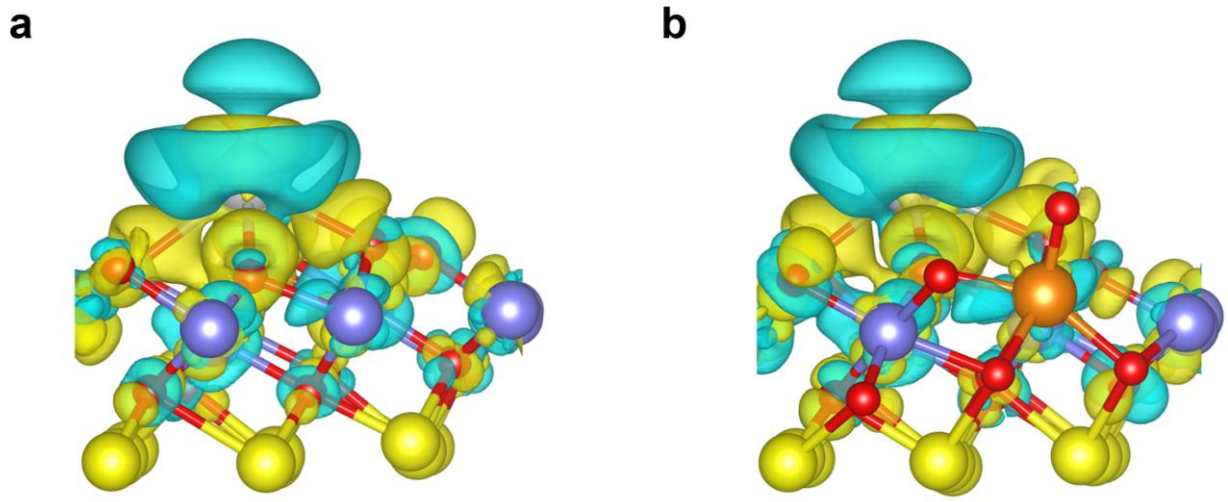

Figure S42. 3D charge difference of unanchored (a) and anchored (b) La-O structure.

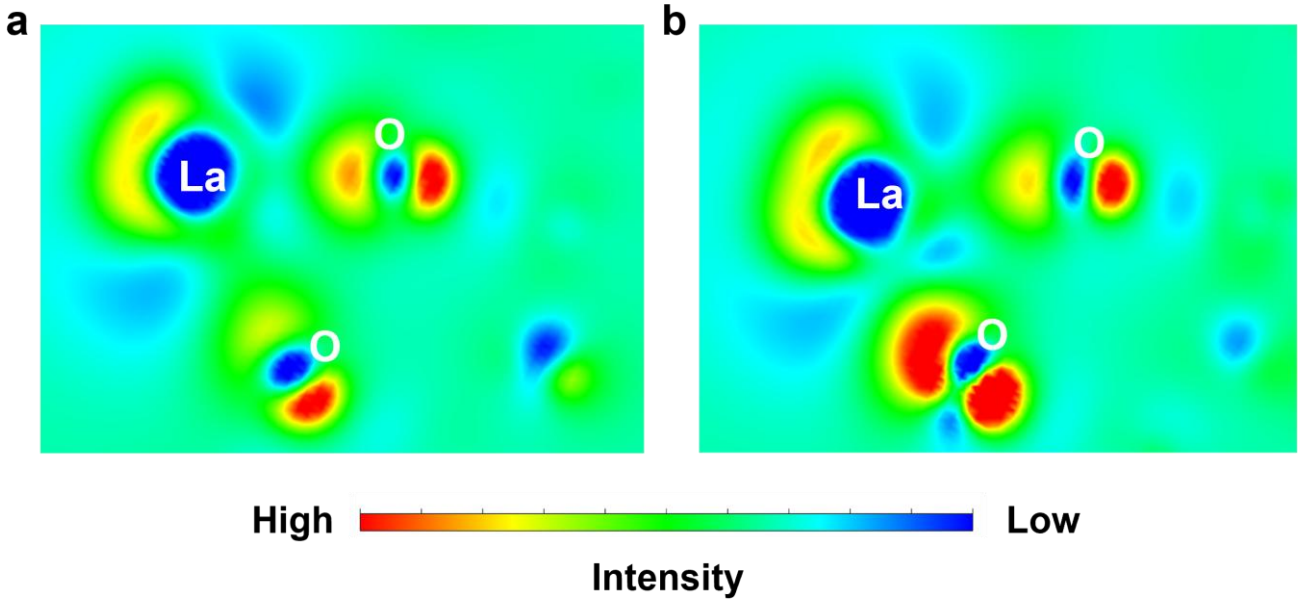

Figure S43. The 2D charge difference for a slice along the plane passing through O-La-O in unanchored La-NCM (a) and DA-NCM (b).

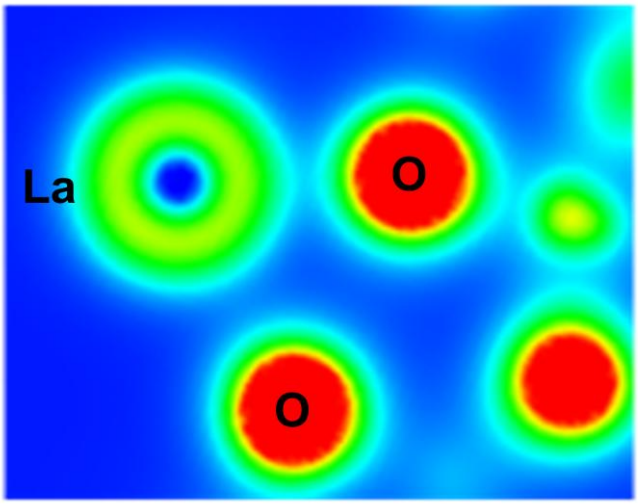

Figure S44. 2D slices of the charge density distribution of unanchored La-O structure.

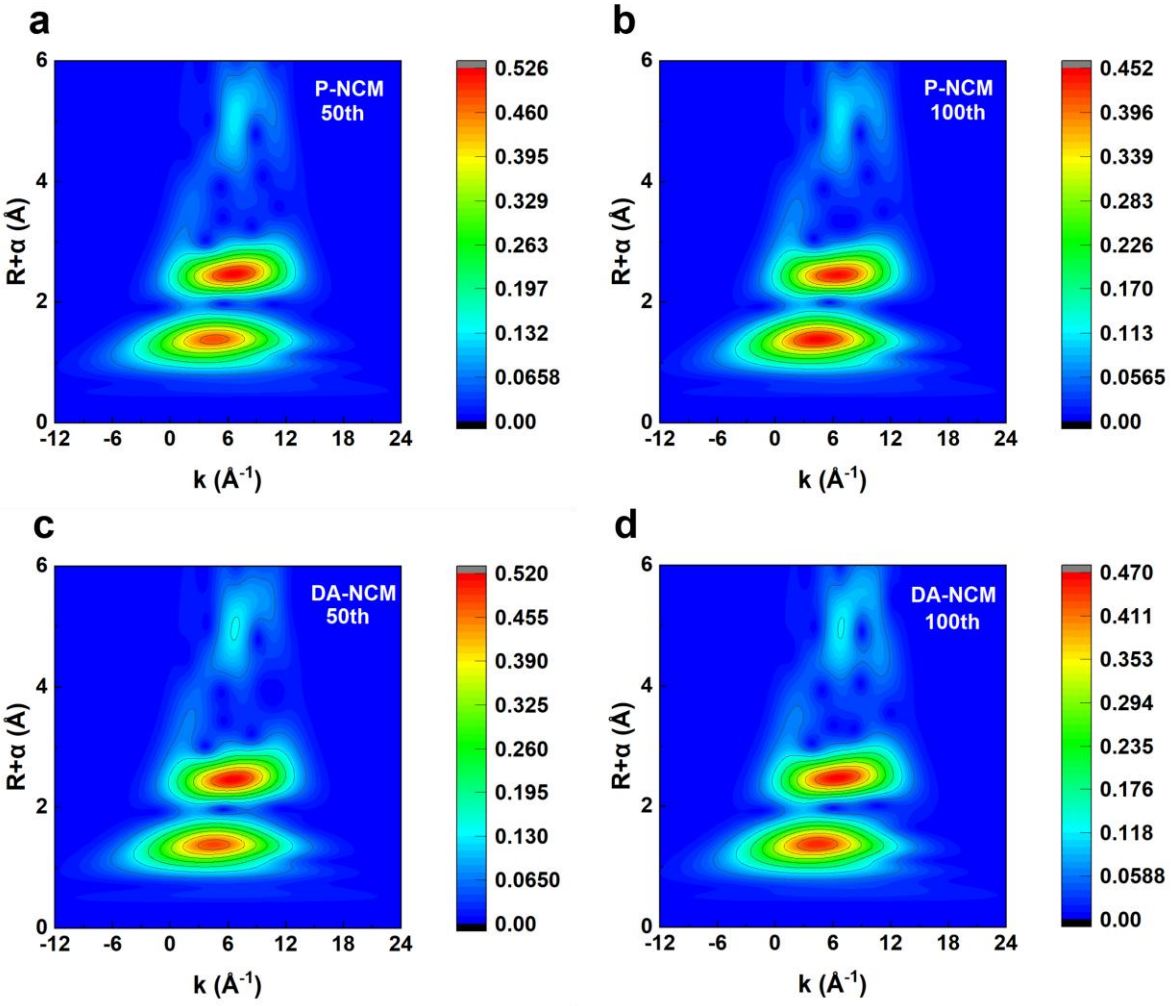

Figure S45. The wavelet-transformed EXAFS of cycled P-NCM (a, b) and DA-NCM (c, d).

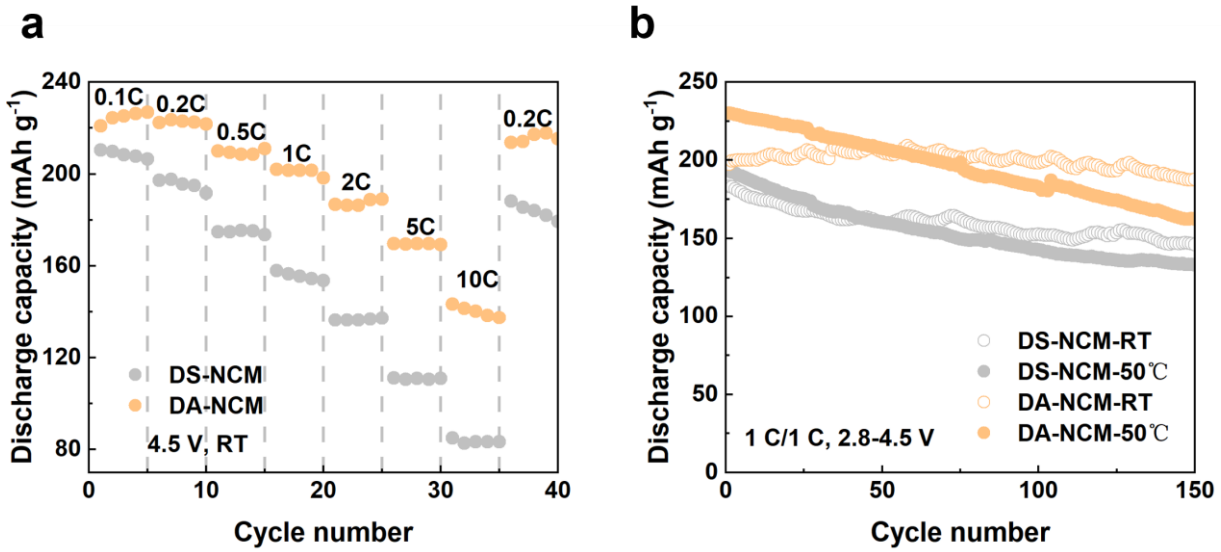

Figure S46. Rate performance (a) and cycle performance (b) of DS-NCM and DA-NCM.

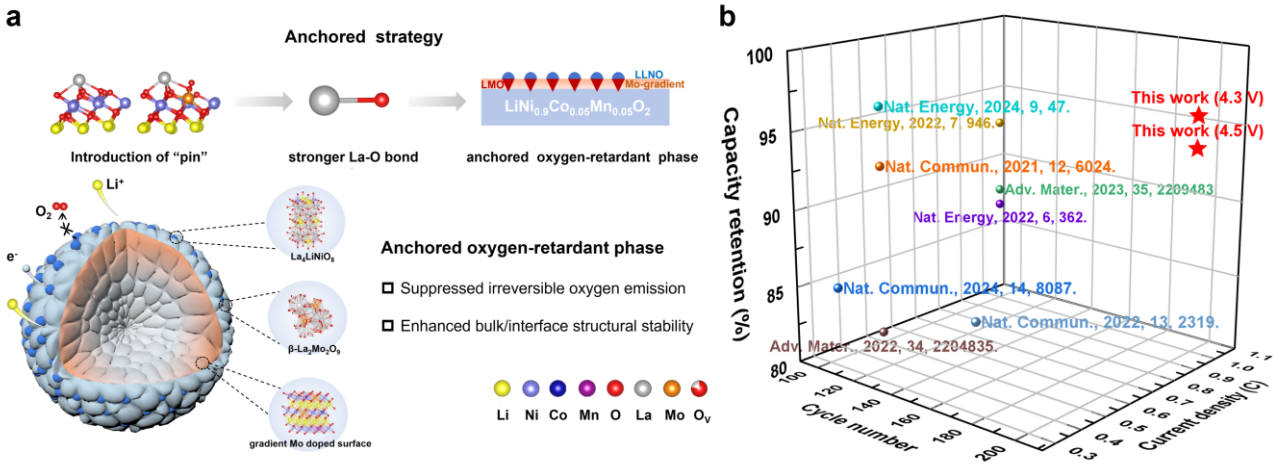

Figure S47 **(**a) Schematic illustrations of anchored oxygen-retardant phase strategy. (b) Comparison of capacity retention between DA-NCM and modified materials from other references.

Table S1. Rietveld Refined crystallographic parameters of XRD for P-NCM, La-NCM and DA-NCM.

Samples	a/Å	c/Å	V/Å	Ni^{2+} in Li site	$I_{(003)}/I_{(104)}$	R_{wp}
P-NCM	2.8687	14.1668	101.040	3.648%	1.376	0.098
La-NCM	2.8697	14.1688	101.052	1.781%	1.479	0.104
DA-NCM	2.8721	14.1830	101.323	1.389%	1.672	0.095

Table S2. Rietveld Refined crystallographic parameters of NPD for P-NCM, La-NCM and DA-NCM.

Samples	a/Å	c/Å	V/Å	Ni^{2+} in Li site	R_{wp}
P-NCM	2.8729	14.1853	101.396	1.812%	0.077
La-NCM	2.8724	14.1906	101.398	1.564%	0.067
DA-NCM	2.8732	14.1864	101.427	1.481%	0.043

Table S3. The intensity ratio of (003) and (104) peaks of all the as-prepared samples at a scan rate of 9° min^{-1}.

Samples	003 peak areas	104 peak areas	$I_{(003)}/I_{(104)}$
P-NCM	3657	2569	1.42
LM03-NCM	3303	2186	1.51
DA-NCM	3016	1901	1.58
LM10-NCM	2588	1679	1.54
La-NCM	3187	2223	1.43
Mo-NCM	2204	1605	1.37

Table S4. Comparison in electrochemical performances of DA-NCM under different voltages with the recent similar-focused literatures[1-10].

Bulk material	Modification strategy	Test condition	Cycle number	Capacity retention	Reference
$LiNi_{0.9}Co_{0.05}Mn_{0.05}O_2$	Anchored oxygen-retardant strategy	2.8-4.3 V, 1C, RT 2.8-4.5 V, 1C, RT 2.8-4.3 V, 1C, 50℃	200	~95.7% ~93.6% ~91.5%	This work
$LiNi_{0.8}Co_{0.1}Mn_{0.1}O_2$	Co_xB-coating	3.0-4.4 V, 1C, RT	100	~87%	[1]
$LiNi_{0.8}Co_{0.1}Mn_{0.1}O_2$	$La_2Mo_2O_9$-coating	2.7-4.5 V, C/3, RT	100	~84.8%	[2]
$LiNi_{0.9}Co_{0.05}Mn_{0.05}O_2$	La_4LiNiO_8-coating	2.8-4.5 V, 1C, RT	100	~88.07%	[3]
$LiNi_{0.9}Mn_{0.1}O_2$	Mo-doping	2.7-4.4 V, 0.5C, RT	100	~92.8%	[4]
$LiNi_{0.8}Co_{0.2}O_2$	concentration gradient strategy	2.8-4.4 V, 0.5C, RT	100	~92%	[5]
$LiNi_{0.83}Co_{0.11}Mn_{0.06}O_2$	Li_2MoO_4-coating and Mo-doping	2.7-4.3 V, 1C, RT	100	~90.22%	[6]
$LiNi_{0.6}Co_{0.2}Mn_{0.2}O_2$	polyrotaxane-co-poly(acrylic acid) polymer-coating	2.5-4.5 V, 0.5C, RT	100	~80.7%	[7]
$LiNi_{0.88}Co_{0.09}Mn_{0.03}O_2$	Al/Zr co-doping	2.8-4.4 V, 0.5C, RT	150	~83.4%	[8]
$LiNi_{0.9}Co_{0.05}Mn_{0.04}5Nb_{0.005}O_2$	F–Co-washed	2.7-4.3 V, 0.5C, RT	100	~95.9%	[9]
$LiNi_{0.8}Co_{0.15}Al_{0.05}O_2$	$Li_5La_3Nb_2O_{12}$-coating and Nb-doping	2.7-4.5 V, 1C, RT	200	~74.3%	[10]

Table S5. R_{ct} obtained from the in-situ galvanostatic electrochemical impedance spectroscopy test for P-NCM (a) and DA-NCM (b) at different voltages.

Samples	2.8 V	3.2 V	3.6 V	4.0 V	4.1 V	4.3 V	4.5 V
P-NCM	301.50 Ω	327.06 Ω	320.15 Ω	365.84 Ω	340.30 Ω	339.81 Ω	344.54 Ω
DA-NCM	231.70 Ω	234.17 Ω	243.50 Ω	236.78 Ω	236.36 Ω	239.04 Ω	231.52 Ω

Table S6. The intensity ratio of (003) and (104) peaks of the high-rate cycled NCM, La-NCM and DA-NCM at a scan rate of 9° min^{-1}.

Samples	003 peak areas	104 peak areas	$I_{(003)}/I_{(104)}$
P-NCM	568	517	1.10
La-NCM	788	540	1.46
DA-NCM	866	375	2.31

References

1. Yoon, M. et al. Reactive boride infusion stabilizes Ni-rich cathodes for lithium-ion batteries. *Nat. Energy* ***6***, 362-371 (2021).

2. Dai, Z. et al. Defective oxygen inert phase stabilized high-voltage nickel-rich cathode for high-

energy lithium-ion batteries. *Nat. Commun.* ***14***, 8087 (2023).

3. Wang, L. et al. Regulating Surface Oxygen Activity by Perovskite-Coating-Stabilized Ultrahigh-Nickel Layered Oxide Cathodes. *Adv. Mater.* ***35***, 2209483 (2023).
4. Park, G.-T. et al. Introducing high-valence elements into cobalt-free layered cathodes for practical lithium-ion batteries. *Nat. Energy* ***7***, 946-954 (2022).
5. Liu, T. et al. Rational design of mechanically robust Ni-rich cathode materials via concentration gradient strategy. *Nat. Commun.* ***12***, 6024 (2021).
6. Teng, T. et al. Simultaneous Li2MoO4 coating and Mo6+ doping improves the structural stability and electrochemical properties of nickel-rich LiNi0.83Co0.11Mn0.06O2. *Appl. Surf. Sci.* ***601***, 154101 (2022).
7. Yang, H. et al. Building a Self-Adaptive Protective Layer on Ni-Rich Layered Cathodes to Enhance the Cycle Stability of Lithium-Ion Batteries. *Adv. Mater.* ***34***, 2204835 (2022).
8. Ou, X. et al. Enabling high energy lithium metal batteries via single-crystal Ni-rich cathode material co-doping strategy. *Nat. Commun.* ***13***, 2319 (2022).
9. Ryu, H.-H. et al. Near-surface reconstruction in Ni-rich layered cathodes for high-performance lithium-ion batteries. *Nat. Energy* ***9***, 47-56 (2023).
10. Zhou, X. a. et al. Utilizing fast ion conductor for single-crystal Ni-rich cathodes to achieve dual-functional modification of conductor network constructing and near-surface doping. *Energy Stor. Mater.* ***52***, 19-28 (2022).